AGU PUBLICATIONS

JGR

Journal of Geophysical Research: Oceans

RESEARCH ARTICLE

10.1002/2014JC010025

# Wave breaking and turbulence at a tidal inlet

**Seth Zippel[1] and Jim Thomson[1]**

[1]Applied Physics Laboratory, University of Washington, Seattle, Washington, USA

**Key Points:**
- Observations of wave breaking and turbulence at a tidal inlet are presented
- Wave breaking models are evaluated in a mixed depth and current environment
- Two surface turbulent dissipation rate scalings are compared

**Correspondence to:**
S. Zippel,
zippelsf@apl.washington.edu

**Citation:**
Zippel, S., and J. Thomson (2015), Wave breaking and turbulence at a tidal inlet, *J. Geophys. Res. Oceans*, *120*, doi:10.1002/2014JC010025.

Received 4 APR 2014
Accepted 6 JAN 2015
Accepted article online 14 JAN 2015

**Abstract** Field measurements collected with surface drifters at New River Inlet (NC, USA) are used to characterize wave breaking and turbulence in the presence of currents. Shoreward wave evolution is affected by currents, and breaking is observed in deeper water with opposing currents (ebb tides) relative to the following currents (flood tides). Wave dissipation models are evaluated with observed cross-shore gradients in wave energy flux. Wave dissipation models that include the effects of currents are better correlated with the observations than the depth-only models. Turbulent dissipation rates measured in the breaking regions are used to evaluate two existing scaling models for the vertical structure and magnitude of turbulent dissipation relative to wave dissipation. Although both describe the rapid decay of turbulence beneath the surface, exponential vertical scaling by water depth is superior to power law vertical scaling by wave height.

## 1. Introduction

Breaking waves suspend sediments and drive the circulations that cause nearshore morphology [e.g., *Wright and Short*, 1984; *Lippmann and Holman*, 1990; *Gallagher et al.*, 1998]. At inlets, this process is modified by tidal currents, which affect wave propagation and alter circulation patterns. Complex feedbacks exist between the waves and the currents. For example, radiation stress from wave breaking can be a leading order term in the momentum balance [*Olabarietta et al.*, 2011], and, during extreme conditions, can trap water inside an inlet during ebb tides [*Orescanin et al.*, 2014]. In addition, momentum from wave breaking can enhance shoreward flows during flood tides [*Wargula et al.*, 2014].

The present study focuses on wave shoaling in the presence of currents, including wave breaking and the resulting turbulence. The frequency integrated wave action balance in the presence of a current $\mathbf{u}$ is [*Kirby*, 1984]:

$$\frac{\partial}{\partial t}E+\nabla\cdot E\left(\mathbf{C_g}+\mathbf{u}\right)=-D, \tag{1}$$

where $E=\rho g H_s^2/8$ is wave energy defined using significant wave height $H_s$, $t$ is time, $\mathbf{C_g}$ is group velocity, $\nabla$ denotes a horizontal spatial derivative, $\mathbf{u}$ is water velocity, and $D$ is the bulk wave energy dissipation (loss) rate. The frequency integrated wave action balance replaces $E/\omega$ in the wave action balance, with $E$, and the nonlinear source/sink term is dropped. (The absolute frequency is $\omega$.) This describes the total wave energy in a natural wave spectrum, however it obscures the known nonlinearities that transfer energy between spectral components during shoaling [*Elgar et al.*, 1995] and breaking [*Herbers et al.*, 2000].

The linear dispersion relation for frequency $\omega$ depends on reference frame, such that:

$$\omega=\sigma+\mathbf{u}\cdot\mathbf{k}, \tag{2}$$

where $\sigma=\sqrt{gk\tanh(kd)}$ is the intrinsic (stationary to water) frequency of the wave, $\omega$ is the absolute (stationary to ground) frequency of the wave, $d$ is depth, and $\mathbf{u}\cdot\mathbf{k}$ is the frequency adjustment due to currents.

Waves shoal against an opposing current because of a change in wave speed over ground $C_g-u$ (for colinear $C_g$ and $u$), similar to how waves shoal in shallow water as the group velocity $C_g$ decreases due to depth decreasing depth $d$. *Mei* [1989] derives the wave blocking case for all depths using the linear dispersion equation, showing the phase speed becomes complex for $-u=C/2$, where $C$ is the phase speed. However, wave blocking is also commonly derived from the wave action balance, where the wave height is undefined when the current is equal in magnitude and opposite in direction to the group velocity $C_g$ [*Chawla and*

*Kirby*, 2002]. For deep water waves, the two derivations are in agreement as $C_g = C/2$, but the shallow water blocking case is less clear.

The application of the wave action balance to wave blocking is problematic since the equation holds true along raypaths, which become caustic in the wave blocking case. However, waves encountering a current are likely to shoal sufficiently that breaking, via over steepening, occurs before the blocking point is reached. Another effect of currents is to focus wave energy, via refraction, which leads to nonlinear statistics that increase the chances for large steep waves (and thus increase breaking probabilities) [*Janssen and Herbers*, 2009].

### 1.1. Wave Breaking (Steepness) Parameters

Wave breaking has long been tied to wave steepness, as given by $Hk/2$ [e.g., *Stokes*, 1880], and bulk values of $Hk/2 \sim 0.15$ are typical for strong breaking conditions [*Banner et al*., 2000]. *Miche* [1944] derived a steepness limitation on breaking $H/L = 0.14\tanh(\pi d/L)$, which is often approximated:

$$\gamma = \frac{H}{d}, \tag{3}$$

in shallow water ($kd < \pi/10$). This shallow water limit has been applied to random waves using $H_s$ or $H_{rms}$ and used extensively to diagnose surf zone breaking [e.g., *Iverson*, 1952; *Bowen et al*., 1968; *Méhauté et al*., 1968; *Longuet-Higgins*, 1970; *Thornton and Guza*, 1982, 1983]. Limiting values for breaking, $\gamma_{brk}$, are commonly between 0.3 and 0.8, although values up to 1.6 have been observed *Sénéchal* [2003].

*Chawla and Kirby* [2002] showed that wave steepness remains the limiting parameter in the presence of a current, and that the centroid wave number $\bar{k}$ is useful in determining a bulk steepness. Therefore, they modified the *Miche* [1944] parameter to:

$$\gamma = \frac{H\bar{k}}{\tanh(\bar{k}d)}. \tag{4}$$

When waves oppose currents, $\bar{k}$ increases (equation (2)), and the steepness parameter will increase. This approach is valid in all depth cases, including shallow and deep limits.

### 1.2. Wave Dissipation Models

When a wave breaks, wave energy is lost at a rate $D$. Several models have been developed to estimate $D$ for a breaking region. *Battjes and Janssen* [1978] modeled breaking as a bore (i.e., hydraulic jump) and described the energy loss as the difference in hydraulic head on either side of the bore. This model has been updated more recently by *Janssen and Battjes* [2007]. They found the dissipation rate $D$, as a function of wave height $H$, to be:

$$D(H) = \frac{B}{4}\rho g f \frac{H^3}{d}, \tag{5}$$

where $B$ is a constant of order 1, and $f$ is frequency. They then formulated the bulk wave energy dissipation for a random wavefield based on a maximum height criterion, and fraction of breaking $Q_b$,

$$\langle D_{JB07} \rangle = \frac{\beta 3\sqrt{\pi}}{16}\rho g \bar{f} Q_b \frac{H_{rms}^3}{d}, \tag{6}$$

where $\bar{f}$ is the average frequency. Breaking fraction $Q_b$ is found using the relation:

$$\frac{1-Q_b}{\ln(Q_b)} = -\left(\frac{H_{rms}}{H_m}\right)^2. \tag{7}$$

This model implicitly assumes a wave height distribution with no waves above a maximum wave height $H_m$, determined from the *Miche* [1944] steepness parameter. However, *Thornton and Guza* [1983] measured a Rayleigh distribution of breaking wave heights in the surf zone, rather than the truncated Rayleigh distribution implied in the *Battjes and Janssen* [1978] formulation. Therefore, *Thornton and Guza* [1983] proposed a different bulk dissipation as:

$$\langle D_{TG83}\rangle = \int_0^\infty D(H)W(H)\rho(H)\mathrm{d}H, \tag{8}$$

where $\rho(H)$ is the probability distribution function of all wave heights, and $W(H)$ is a weighting function such that $W(H)\rho(H)$ is the probability distribution function of broken wave heights. Note that the fraction of breaking $Q_b$ is then estimated as $Q_b = \int_0^\infty W(H)\rho(H)\mathrm{d}H$. Assuming a Rayleigh distribution, $\rho(H)$ is defined as:

$$\rho(H) = \frac{2H}{H_{rms}^2}\exp\left[-\left(\frac{H}{H_{rms}}\right)^2\right], \tag{9}$$

and the empirical weighting function $W(H)$ is defined as:

$$W(H) = \left(\frac{H_{rms}}{\gamma d}\right)^2\left\{1-\exp\left[-\left(\frac{H}{\gamma d}\right)^2\right]\right\}. \tag{10}$$

The authors state the restriction $W(H) \leq 1$ such that fraction of breaking retains the necessary physical limit, $Q_b \leq 1$, but do not functionally restrict the weighting function. The full wave dissipation function is then:

$$\langle D_{TG83}\rangle = \frac{3\beta\rho}{32\sqrt{\pi}}\rho g\bar{f}\frac{H_{rms}^5}{\gamma^2 h^3}\left\{1-\left[1+\left(\frac{H_{rms}}{\gamma d}\right)^2\right]^{-5/2}\right\}. \tag{11}$$

*Chawla and Kirby* [2002] extended this model by including their steepness parameter $\gamma = H_{rms}\bar{k}/\tanh(\bar{k}d)$ (see section 1.1) into equation (10), and therefore altering equation (8). In addition, they used a new dissipation function $D(H)$ based on a modified length scale that is valid in deep water,

$$D(H) = \frac{\beta}{8\pi}\rho g k H^3\left(\sqrt{\frac{gk}{\tanh(kd)}}\right). \tag{12}$$

Both the amended dissipation function and the steepness function reduce to the previously posed forms in shallow water. *Chawla and Kirby* [2002] amended the *Battjes and Janssen* [1978] model as:

$$\langle D_{CK1}\rangle = \frac{\beta}{8\pi}\rho Q_b\left(\sqrt{\frac{(g\bar{k})^3}{\tanh(\bar{k}d)}}\right)H_{rms}^3, \tag{13}$$

which will hereafter be referred to as CK1. Here, $H_{rms}$ replaces the $H_m$ used in *Chawla and Kirby* [2002] to reflected the updated model of *Janssen and Battjes* [2007]. The full *Chawla and Kirby* [2002] amended *Thornton and Guza* [1983] dissipation model is written:

$$\langle D_{CK2}\rangle = \frac{3\beta\rho}{32\sqrt{\pi}}\left(\sqrt{\frac{(g\bar{k})^3}{\tanh(\bar{k}d)}}\right)H_{rms}^5\left\{1-\left[1+\left(\frac{\bar{k}H_{rms}}{\gamma\tanh(\bar{k}d)}\right)^2\right]^{-5/2}\right\}, \tag{14}$$

which will hereafter be referred to as CK2.

### 1.3. Wave Breaking Turbulence

The energy lost from waves during breaking is transferred into turbulent kinetic energy (TKE), mean kinetic energy, bubbles, and sound [*Longuet-Higgins*, 1970; *Battjes and Janssen*, 1978; *Lamarre and Melville*, 1991]. Previous studies have shown a correlation between wave breaking dissipation, $D$, and turbulent dissipation rates, $\epsilon$, but the two often differ by a factor of 100 [*Feddersen*, 2012a; *Thomson*, 2012]. *Feddersen* [2012a] attributed the differences in magnitude to measurements being taken below the areas of highest dissipation, as TKE is expected to decay rapidly beneath a breaking crest. However, *Thomson* [2012] measured turbulent dissipation rates in the top 60 cm of the water column in the surf zone and still observed a large difference in magnitude between the wave dissipation rate and the TKE dissipation rate. However, it is noted that the ADCP used in this study could not measure inside the bore.

*Terray et al*. [1996] assumed that turbulent length scales increase linearly below the surface in deep water, such that surface turbulence follows a power law scaling,

$$\frac{\bar{\epsilon} H_s}{G} = A_T \left( \frac{z}{H_s} \right)^{\lambda}, \tag{15}$$

where $G$ is the surface flux of TKE and $z$ is distance from the mean surface with the surface at $z = 0$ and $\lambda = -2$ is a constant. *Feddersen* [2012a] adapted this power law scaling to the surf zone using $G = dF/dx$, but found it had low skill. *Feddersen* [2012b] derived an exponential scaling based on water depth (as opposed to wave height), formulated as:

$$\frac{\bar{\epsilon} d}{G} = A_F \exp(\alpha \zeta), \tag{16}$$

where $A_F$ and $\alpha$ are constants, and $\zeta$ is the nondimensional height above the bed $\zeta = z'/d$ ($z' = 0$ at the bed, reversed from the *Terray et al*. [1996] convention). *Feddersen* [2012b] found the exponential scaling to be more skillful than the modified *Terray et al*. [1996] scaling in the surf zone. In addition, the two parameters, $A_F$ and $\alpha$, fit independently, were used to estimate the percentage of wave energy dissipated into the water column. If 100% of the wave energy is dissipated into the water column, then $A_F$ is expected to follow the relationship $\tilde{A}_F = \alpha / \exp(\alpha)$. The ratio of the best fit $A_F$ to the theoretical $\tilde{A}_F = \alpha / \exp(\alpha)$ therefore gives an estimate of the percentage of wave energy dissipated into the water column. We will evaluate the surf zone versions of these scalings, including the constants $A_T$, $\lambda$, $A_F$, and $\alpha$.

This paper presents observations of wave transformation, breaking, and the resulting turbulence at a tidal inlet, and evaluates these observations with the wave and turbulence theories described in section 1. A field site description and methods are presented in section 2. Example drifter tracks, a comparison of wave dissipation models, and a comparison of turbulent dissipation models are shown in section 3. The results are discussed in section 4. Conclusions are stated in section 5.

## 2. Methods

### 2.1. Data Collection

The study site, New River Inlet, was chosen as part of a large collaborative study on inlets. New River Inlet is located south of the Outer Banks near Marine Corps Base Camp Lejeune in North Carolina (USA). High and low tide were in phase with max flood and ebb currents (i.e., a progressive tide). Tide variations from mean sea level were on the order of $\pm 0.5$ m for neap tides and $\pm 1$ m for spring tides. Currents were consistently larger than 1 m/s, and measured as large as 1.5 m/s. The freshwater input from the river was small; the flows were primarily tidal and the currents were approximately vertically uniform. Offshore wave heights during the experiment were typically $H_s \leq 1$ m with peak periods in the 7–9 s range. The beach faces southeast (approximately 140° true).

SWIFT drifters, which are wave following buoys designed for near surface measurements [*Thomson*, 2012], were deployed at the inlet between 26 April and 21 May 2012. The SWIFTs measure wind (using an Airmar PB200); location, drift speed, and waves (using a Qstarz BT-Q1000eX GPS); turbulent dissipation rate (using a Nortek 2MHz Aquadopp HR); take images (using a GoPro Hero); and have local tracking (using Garmin Astro collars). Bathymetry data were collected by the Army Corps FRF LARC survey system on 2 May 2012. Reported water depths were corrected for tides using a pressure gauge located at [$x = -479$ m, $y = -390$] m in a local coordinate system with an origin in the middle of the inlet. Surface currents and positions are estimated as the 5 min averages of GPS time series of velocity and position, respectively. The SWIFT drifts are slightly contaminated by wind drag, approximately 5% of the wind speed [*Thomson*, 2012]. Reported currents are compensated for this 5% wind drift using data from the onboard sonic anemometer.

The SWIFT drift tracks (11 total, see Table 1) processed for this study are shown in Figure 1b. SWIFTs deployed on ebb tides from inside the inlet (green tracks in Figure 1b) preferentially followed the channels out the inlet and once offshore they followed the wind and wave directions. Breaking on ebb tides was observed at the ends of channels where currents were large (Figure 1a). Breaking on ebb tides also occurred over the shallow shoals near North Topsail Island and Onslow Beach.

Flood deployments (magenta tracks in Figure 1b) resulted in a more diffuse pattern, in which SWIFTs would rarely drift into the inlet when dropped more than approximately 700 m from the river mouth. Breaking on flood tides occurred primarily on the shoals near North Topsail Island and Onslow Beach, and the shallow bar in between the two dredged channels.

**Table 1.** SWIFT Drift Deployments With Manually Reviewed Video Data

| Track Start Time | SWIFT | Tide | Windspeed (m/s) | Offshore $H_s$ (m) | Offshore $D_a$ (°) | Breaking (X,Y) |
|---|---|---|---|---|---|---|
| 20 May 2012-12:22 | 04 | Ebb | 3.5 | 0.76 | 5.5 | 388, −47 |
| | | | | | | 625, 22 |
| 30 Apr 2012-10:07 | 06 | Ebb | 4.3 | 0.53 | 3.5 | |
| 17 May 2012-10:57 | 06 | Ebb | | 0.67 | 5.8 | 429, 460 |
| | | | | | | 665, 785 |
| 17 May 2012-11:42 | 06 | Ebb | | 0.70 | 5.8 | 717, 213 |
| 18 May 2012-11:32 | 04 | Ebb | 5.7 | 0.90 | 4.2 | |
| 18 May 2012-07:02 | 04 | Flood | 4.7 | 0.92 | 3.9 | 505, −111 |
| | | | | | | 359, −202 |
| | | | | | | 255, −234 |
| 13 May 2012-12:47 | 04 | Flood | 5.0 | 0.82 | 3.8 | 696, 168 |
| | | | | | | 399, 185 |
| | | | | | | 280, 179 |
| 13 May 2012-12:52 | 03 | Flood | 5.3 | 0.82 | 3.8 | 471, −249 |
| | | | | | | 350, −214 |
| 08 May 2012-12:22 | 06 | Flood | 2.4 | 0.68 | 4.6 | |
| 12 May 2012-08:57 | 02 | Ebb | | 0.49 | 5.8 | |
| 12 May 2012-09:07 | 04 | Ebb | 2.2 | 0.49 | 5.8 | 441, 422 |

All of the other SWIFT estimates, described below, are also processed in 5 min bursts to make ensemble estimates. During a 5 min burst, a SWIFT may drift as much as 300 m, and thus the resulting ensemble estimates are not well localized in space. The nonlocalization in space introduced errors in the depth used for estimating bulk parameters. Also, the underlying time series will not have strict stationarity. Still, ensemble estimates along the drift tracks show strong gradients in wave spectra, breaking fraction, and turbulence levels. These gradients, $d/dx$, exceed the errors introduced via coarse resolution $dx$ by at least a factor of 10 in the regions of interest.

### 2.2. Wave Spectra, $E(\sigma)$

SWIFT wave spectra were estimated from horizontal velocities collected at 5 Hz, following the method described in *Herbers et al.* [2012]. Low-frequency noise in the horizontal velocity time series was reduced by using a 20 s high-pass RC filter. Spectra are found with the Welch method, using a Hamming taper on 128 s windows with 75% overlap for each 512 s burst of filtered, detrended velocity data. Adjacent frequency bands are then merged to reduce noise. The horizontal spectra were used to calculate the sea surface elevation power spectral density using known depth and linear wave theory with the equation:

$$\frac{E(\sigma)}{\rho g} = \frac{(S_{uu}+S_{vv})C^2}{g^2}, \tag{17}$$

where $E(\sigma)$ is the sea surface elevation energy spectral density, $S_{uu}$ and $S_{vv}$ are the horizontal velocity energy spectral density, $C$ is the wave celerity, and $g$ is acceleration due to gravity. Because SWIFT measurements are wave following, $\sigma$ is the moving frame intrinsic frequency, as opposed to the absolute frequency

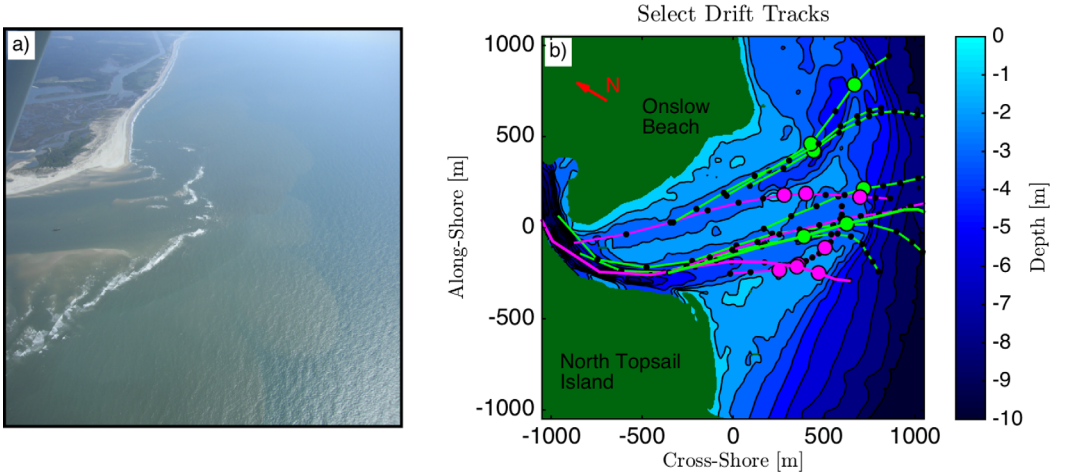


**Figure 1.** (a) New River Inlet, NC during low tide. Wave breaking can be seen on the shallow shoals on the sides of the inlet as well as across the channel mouths. Photo: Gordon Farquharson. (b) Bathymetry contours (1 m) and SWIFT drifter tracks for which onboard images were processed. Bathymetry data were collected on 2 May 2012 by the Army Corps FRF LARC survey system. The map is rotated into a cross-shore, alongshore coordinate system; a 58° rotation from true north. Ebb tracks are shown in light green, floods tracks are shown in magenta. Thick colored lines mark the tracks shown in Figures 2, 3, 5, and 6. Black dots denote the center of 5 min average positions. Colored circles show locations of where more than one breaking wave was identified for the 5 min burst. A total of 11 tracks are plotted. Drift days, break point locations, and offshore conditions are shown in Table 1.

$\omega$ (equation (2)). Wave spectra giving a significant wave height of less than 0.2 m, and with a peak period greater than 22 s are discarded. Wave direction, $\mathbf{k}/k$, is found per frequency component using the $a_2$ and $b_2$ spectral coefficients with $a_2=(S_{xx}-S_{yy})/(S_{xx}+S_{yy})$, $b_2=2C_{xy}/(S_{xx}+S_{yy})$ and $\tan(2\theta)=b_2/a_2$ [*Herbers et al.*, 2012]. Wave direction therefore has 180° ambiguity, and are assumed to be propagating toward shore. However, directions near grazing to shore can be difficult to analyze.

To simplify analysis, avoid confusion between reference frames, and make a more direct connection to a bulk wave steepness, wave energy spectra are converted to wave number spectra $E(k)$. The conversion requires adjusting the bandwidth normalization of $d\sigma$ to $dk$, and the result is a nonuniform mapping to $k$. A centroid wave number $\bar{k}$ is defined as the energy weighted average of each spectrum. Wave numbers $k$ are invariant between reference frames, however the centroid wave number $\bar{k}$ does change along a drift track because the wave energy changes during breaking.

Each full spectrum is used to calculate wave energy fluxes $F=(1/\rho)\int E(\sigma)[C_g(\sigma)+\mathbf{u}]d\sigma$. Cross-shore energy flux gradients are estimated as $\mathrm{d}F/\mathrm{d}x=(1/\rho)\int\{\Delta E(\sigma)[C_g(\sigma)+u]_x/\Delta x\}\mathrm{d}\sigma$, where the subscript $x$ denotes the cross-shore component in the rotated coordinate system. The forward differenced (down wave) wave gradient is evaluated at the down stream location to be consistent with measured turbulent dissipations.

### 2.3. Breaking Fraction, $Q_b$

Breaking rates were counted by manual review of GoPro images collected onboard the SWIFTs at 1 Hz. Only waves breaking over, or extremely close to, the SWIFT hull were counted. Because manual review of all images (approximately 1.5 million) was impractical, and automated methods were incomplete, a select few tracks were counted (11 tracks total). GoPro clocks were synced before each deployment with visual images of wristwatches. These were confirmed with written records of SWIFT deployment times in order to sync GoPro timestamps with the GPS time recorded onboard.

The number of breaking waves, $n$, counted during a 5 min burst is converted to a breaking fraction by:

$$Q_b=\frac{2\pi}{\bar{\sigma}}\frac{n}{\mathcal{T}}, \tag{18}$$

where $\bar{\sigma}$ is the intrinsic frequency associated with the centroid wave number of the energy spectrum and $\mathcal{T}$ is the duration of the time series (= 5 min = 300 s). This assumes that breaking is predominantly occurring at the centroid of the spectrum. The maxima of $Q_b$ along a given drifter track is used to define the breakpoint of track, which is important context for the wave and turbulence estimates.

### 2.4. Turbulent Dissipation Rate Profiles, $\epsilon(z)$

Turbulent dissipation rates are calculated using a one-sided, top-down, second-order structure function method: a direct eddy scale approach described in *Wiles et al.* [2006], *Gemmrich* [2010], and *Thomson* [2012]. The structure function describes the energy cascade proposed by *Kolmogorov* [1941], in which velocity differences scale with separation distances $r$ as proxy for the eddy scales:

$$SF(z,r)=\langle(u'(z)-u'(z+r))^2\rangle=C_n^2\bar{\epsilon}^{\frac{2}{3}}r^{\frac{2}{3}}. \tag{19}$$

The turbulent velocity profiles $u'(z)$ are measured with an Aquadopp HR at depths below the surface $z$, in a wave following reference frame. The theoretical turbulent dissipation rate $\epsilon$ is related with a constant $C_n^2=2.1$. Calculated structure function values are fit to $r^{\frac{2}{3}}$ using MATLAB's robust fit algorithm giving a slope $A$ and an intercept $N$:

$$SF(z,r)=A(z)r^{\frac{2}{3}}+N. \tag{20}$$

Intercept values $N$ are expected to follow a Gaussian distribution related to the noise in the velocity measurement. Burst average turbulent dissipation rates $\bar{\epsilon}$ are then estimated from the slope coefficients $A$ at every depth $z$ using:

$$\bar{\epsilon}(z)=C_n^{-3}A(z)^{\frac{3}{2}}. \tag{21}$$

## 3. Results

### 3.1. Wave Evolution

An example of wave transformation with an opposing current is shown in Figure 2. Wave number spectra show increased shoaling in low wave number bands, consistent with the results from *Chawla and Kirby* [2002].

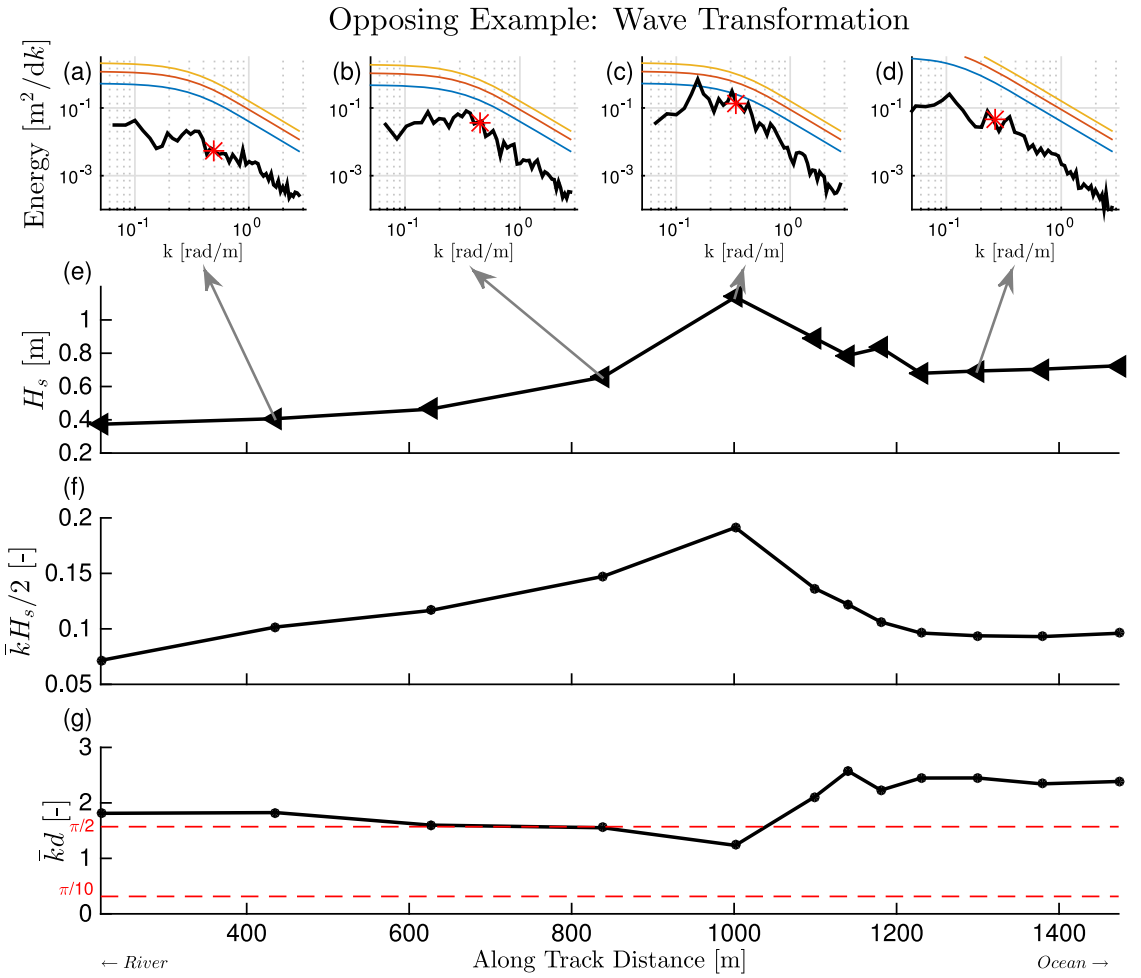


**Figure 2.** Example ebb SWIFT drift on 20th May 2012. The SWIFT was deployed (left) inside the inlet and (right) drifted offshore as time progressed. (a–d) Wave number spectra, and centroid wave numbers $\bar{k}$ with a red asterisk. Steepness limitations (equation (4)) for $\gamma$=0.2, 0.3, 0.4 are shown on the spectra in blue, orange, and yellow, respectively. (e) Significant wave height. (f) Wave steepness. (g) Relative wave depth.

Shoreward spectra show a considerable decrease of energy in the lower wave numbers. As a result, centroid wave numbers $\bar{k}$ are increased close to shore. The spectrum in Figure 2c ($x = 1000$ m) shows $E(k)$ exceeds the steepness criterion at low wave numbers. This coincides with the maximum wave steepness and wave height at $x = 1000$ m, all of which will be shown to coincide with the maximum breaking fraction in the next section. The relative wave depth, $\bar{k}d$ is in the intermediate regime at the location of breaking, and increases shoreward. This suggests that the wave breaking is not solely a depth limited process in the presence of an opposing current.

An example of wave transformation with a following current is shown in Figure 3. Here, the signal is largely controlled by the depth. The alongtrack maximum steepness occurs at $x = 500$ m, when the waves are closest to the shallow regime. This will be shown to coincide with maximum breaking fraction in the next section. In addition, the observed spectra in the breaking region, Figure 3c, exceeds the steepness limit for low wave numbers where the steepness limit is flat. This implies the shallow approximation is valid for the overly steep spectral components.

Figure 4 generalizes these examples by showing wave steepness and breaking fraction as a function of depth for the 11 tracks. For following currents, wave steepness is well correlated with depth ($R^2$=0.6, $n = 43$), consistent with waves that propagate into the shallows and break at the shore (or over the surrounding shoals). For opposing currents, however, wave steepness is almost independent of depth ($R^2$=0.1, $n = 79$). This is consistent with waves steepening and breaking against currents at the mouth of the inlet, such that waves are steeper offshore and waves are filtered to be lower steepness onshore. This filtering creates a wide scatter in steepness as a function of depth.

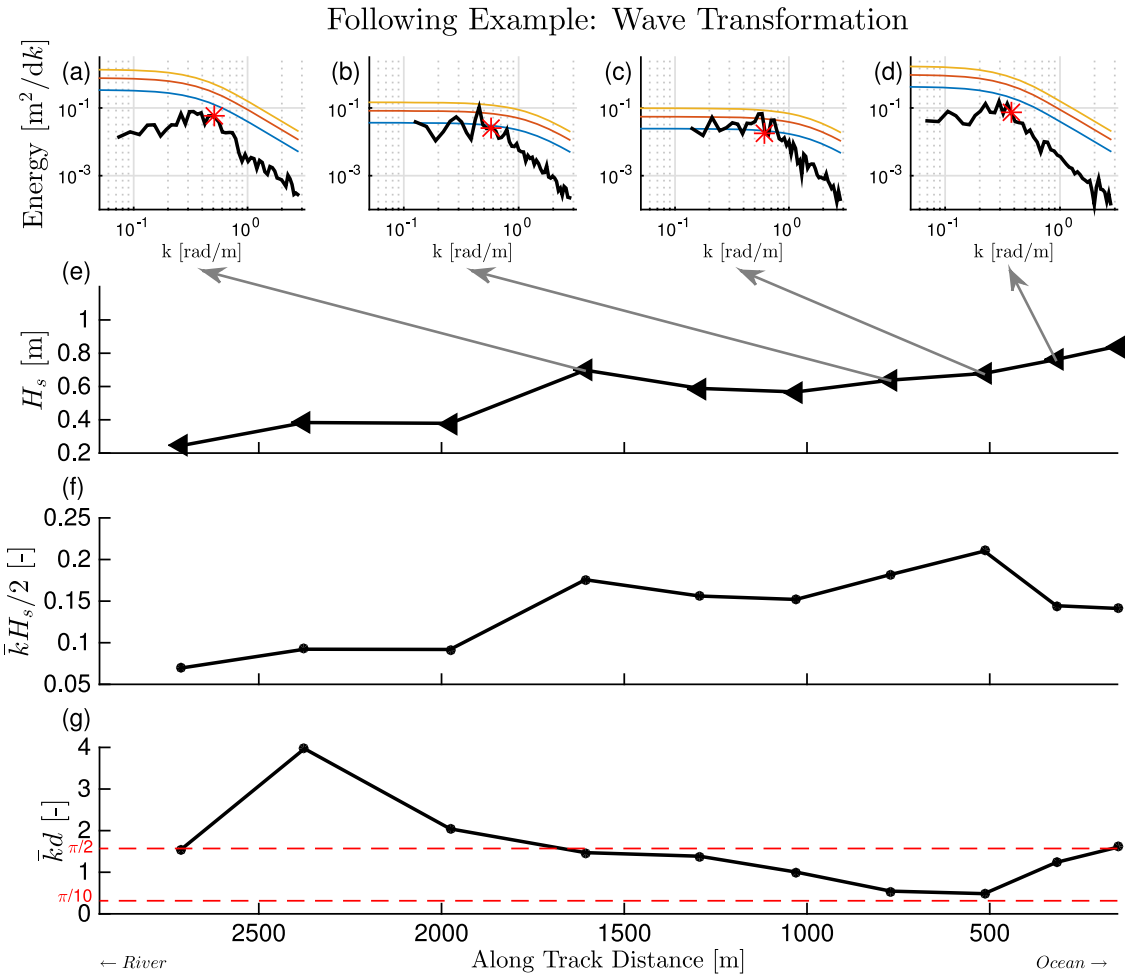


**Figure 3.** Example flood tide SWIFT drift on 13 May 2012. The SWIFT was deployed (right) outside the inlet and (left) drifted onshore as time progressed. (a–d) Wave number spectra, and centroid wave numbers $\bar{k}$ with a red asterisk. Steepness limitations (equation (4)) for $\gamma$=0.2, 0.3, 0.4 are shown on the spectra in blue, orange, and yellow, respectively. (e) Significant wave height. (f) Wave steepness. (g) Relative wave depth.

Similarly, observed breaking fractions $Q_b$ show a strong contrast between following and opposing currents (Figures 4c and 4d). Breaking occurs in shallow water ($d < 2$ m) exclusively with following currents and the breaking fraction is inversely correlated with depth. Breaking occurs in deeper water ($d > 2$ m) with opposing currents and the breaking fraction is uncorrelated with depth.

### 3.2. Wave Breaking

Figure 5 shows wave breaking metrics for the example of Figure 2, where waves break with an opposing current. Three independent wave breaking metrics, wave energy flux gradient, breaking fraction, and turbulent dissipation rates, all indicate breaking at approximately 1000 m alongtrack (Figures 2a–2c). Figure 2a shows wave energy flux is constant offshore, increasing slightly via focusing against the ebb current at the channel mouth, then declining to near zero from breaking. Figure 2b confirms visual identification of breaking waves as $Q_b$ determined from the onboard camera. Figure 2c shows an increase in turbulent dissipation rates coincident with both observed breakers and a change in wave energy flux. The break point at $x = 1000$ m identified with the maximum breaking fraction $Q_b$ is consistent with the maximum along-track steepness (Figure 2).

Figure 5d shows results from the three different wave dissipation models (equations (6), (11), (13), and (14)), as well as the gradient in the observed wave energy flux. Negative energy flux gradients are not shown. All of the models have a similar pattern with maximum wave dissipations between $x = 1000$ m and $x = 1100$ m.

Figure 5e shows the depth profile and observed currents for this example. The breakpoint at $x = 1000$ m is both the location of a peak in the currents and a transition to the shallow depths of the ebb-tidal shoal.

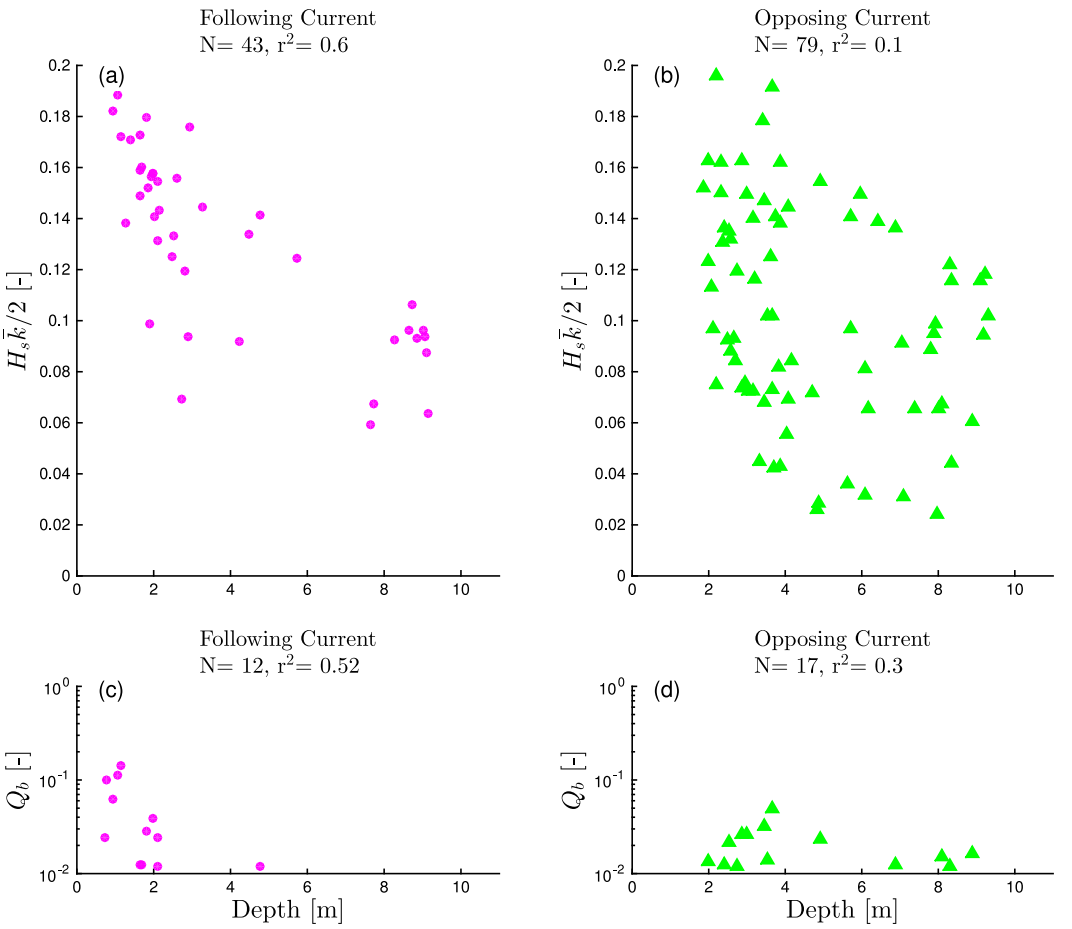


**Figure 4.** Wave steepness, $H_s\bar{k}/2$, is plotted against depth for following (a) and opposing (b) waves and currents. Wave steepness shows a strong correlation with depth on following currents ($r^2=0.59$), but no correlation when waves oppose currents ($r^2=0.07$). Fraction of breaking, $Q_b$ is plotted against depth for following Figure 4c and opposing Figure 4d currents.

Although the waves are clearly not in the shallow regime, according to Figure 2g, the shoal is likely important to the onset of breaking (otherwise the surf zone wave dissipation models of T&G and J&B would not show a similar pattern to the observed gradients of wave energy flux). Other cases of opposing currents are similar and suggest that the effect of the currents is to shift the break point offshore (to deeper water).

Figure 6 shows wave breaking metrics for the example of Figure 3, where waves break with a following current. The decrease in wave energy flux in Figure 6a, the image-based breaking fraction in Figure 6b, and the elevated turbulent dissipation rates in Figure 6c, at $x = 500$ m indicate a breakpoint. This breakpoint is consistent with the wave transformation in Figure 2, and these waves are close to the shallow limit. The wave dissipation models in Figure 6d are scattered around the gradient in observed wave energy flux, and there is negligible difference between models with and without current. The depth profile and observed current in Figure 6e show that breaking occurs exactly at the transition to shallow depths over the ebb-tidal shoal and that currents are relatively week at the break point. Other cases of following currents are similar and suggest that conventional approaches to depth limited breaking are sufficient to describe the observations (i.e., following currents can be neglected, to first order).

Figure 7 evaluates the four different wave dissipation models for all cases, using observed energy flux gradients as ground truth. The models were not tuned, and used arbitrary constants $\gamma=0.4$ and $\beta=0.5$. The current adjusted models from *Chawla and Kirby* [2002] showed slightly improved correlations with observations when compared their depth-only dependent counterparts ($r^2=0.31$ to $r^2=0.36$ and $r^2=0.17$ to $r^2=0.28$). However, the current adjusted model CK2 increased bias, significantly overestimating wave energy dissipation. This bias can be corrected by using a much lower $\beta$, but the required tuning would be

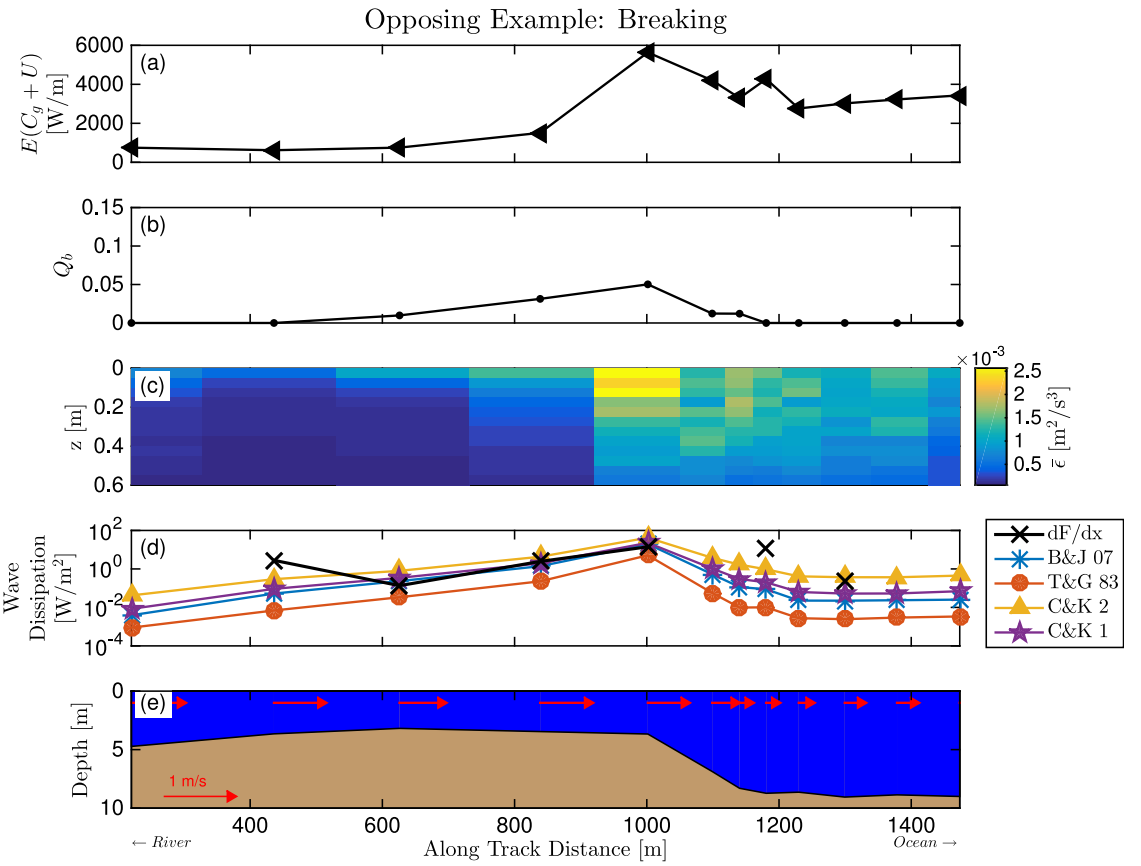


**Figure 5.** Example ebb SWIFT drift on 20 May 2012. The SWIFT was deployed (left) inside the inlet and (right) drifted offshore (right) as time progressed. (a) Wave energy flux. (b) Breaking fraction from onboard images. (c) Turbulent dissipation rates beneath the waves. (d) Three wave dissipation models, as well as the estimated energy flux gradient. (e) The bathymetry and the measurement tidal currents (scaled arrows).

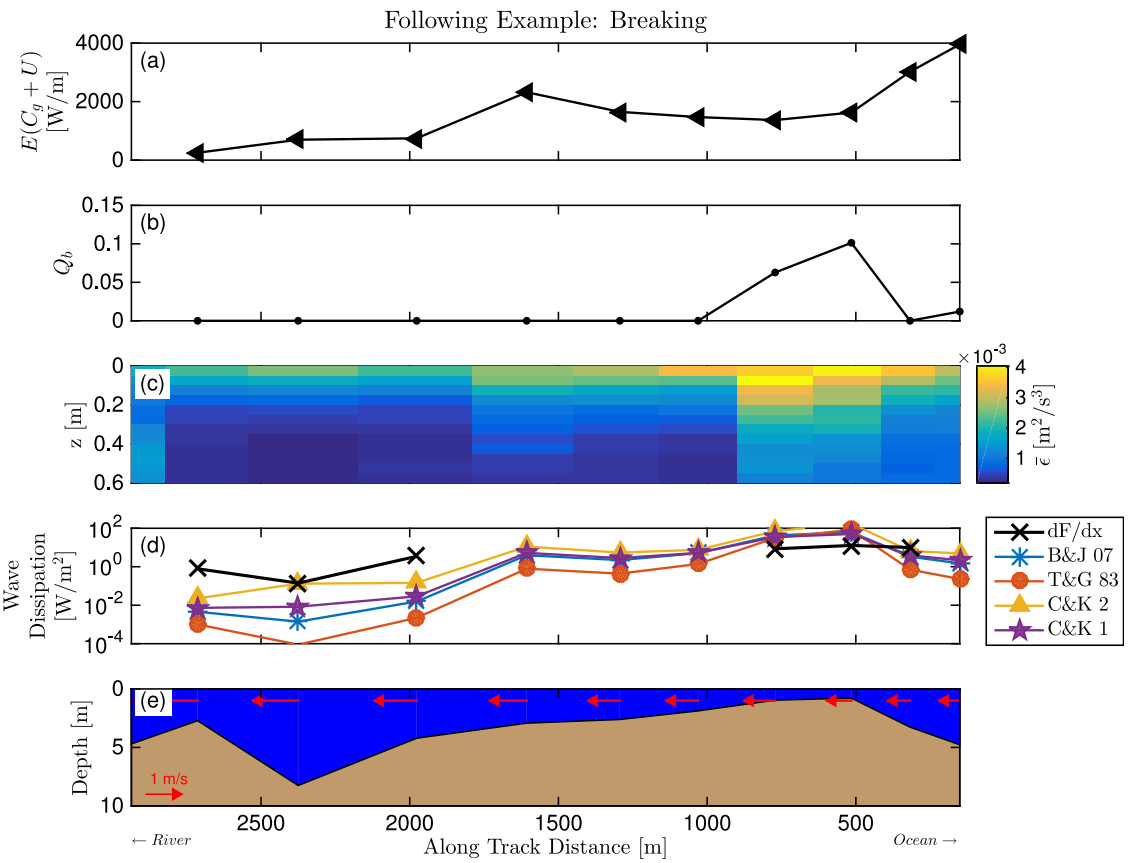


**Figure 6.** Example flood SWIFT drift on 13 May 2012. The SWIFT was (right) deployed offshore and (left) drifted into the river inlet. (a) Wave energy flux. (b) Breaking fraction from onboard images. (c) Turbulent dissipation rates beneath the waves. (d) Three wave dissipation models, as well as the estimated energy flux gradient. (e) The bathymetry and the measurement tidal currents (scaled arrows).

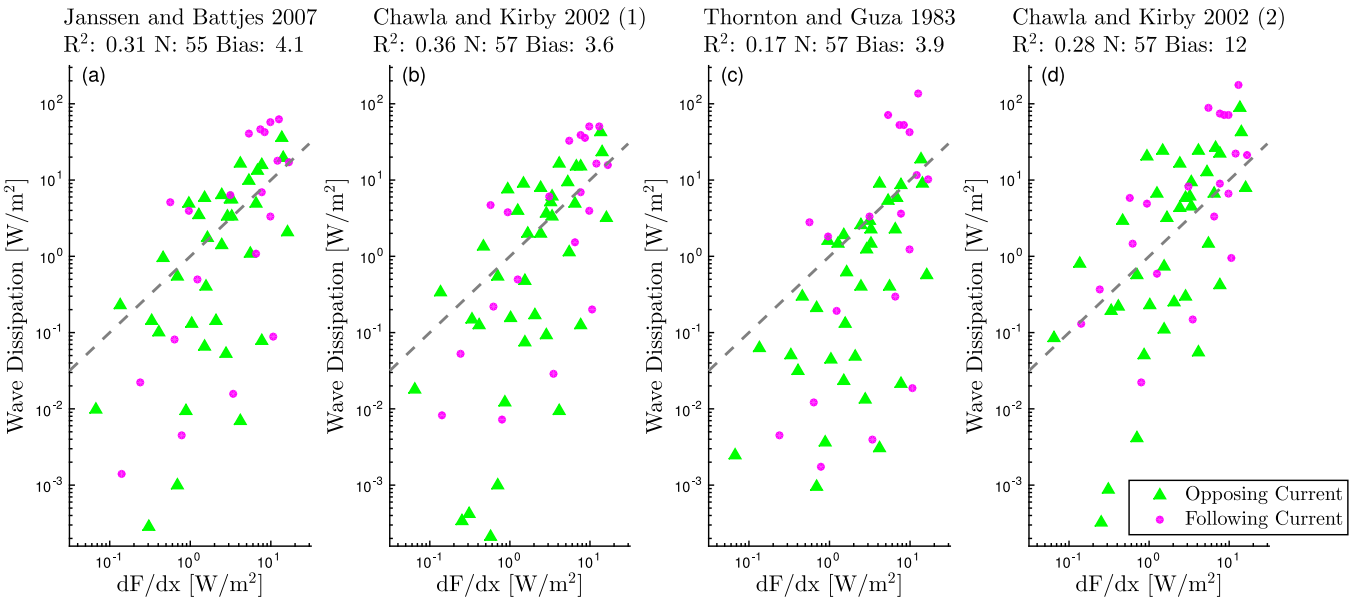


**Figure 7.** The four wave dissipation models (section 1.2) are shown against estimates of wave energy flux gradients. The gray-dashed line represents 1:1. The models were not tuned, and used arbitrary constants $\gamma$=0.4 and $\beta$=0.5. Green triangles represent data taken when waves oppose currents. Magenta circles show data when waves follow currents. The CK1 model has the best skill, $r^2$=0.36 and lowest bias, 3.6 (W/m$^2$). All wave models are biased high when compared to measurements. Errors in the measurement-based wave energy flux gradient estimates are as large as 50% of the estimate. However, the estimates are still useful in evaluating the models because the range of values span two decades.

unphysical. In addition, the JB07 based models show better correlation with the measured flux gradients than the TG83 based models ($r^2$=0.31 and $r^2$=0.36 compared to $r^2$=0.17 and $r^2$=0.28). The generally low correlations of all models are attributed to errors in observed energy flux gradients of up to 50%. However, the estimated energy flux gradients spanning two orders of magnitude are still useful in showing general trends in the models.

Two key parameters for the wave dissipation models, wave steepness and breaking fraction are shown in Figure 8. Figure 8a shows the steepness from *Chawla and Kirby* [2002], which includes currents via the modification of $\bar{k}$. Figure 8b shows conventional steepness in shallow water, without currents. In the *Thornton and Guza* [1983]

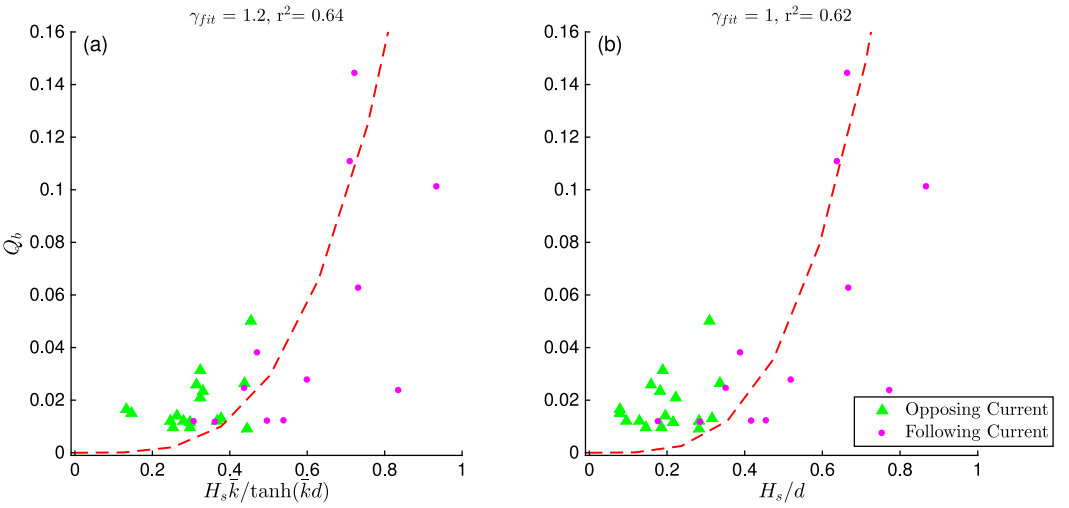


**Figure 8.** Breaking parameters plotted against breaking fraction $Q_b$, shown with the best fit for the weighted Rayleigh distribution of breakers model, using $\gamma$ as the free fitting parameter. Green triangles represent opposing wave/current cases, magenta circles following cases. While the correlation for both breaking parameters are similar, the full steepness parameter shown in plot (a) improves the fit by shifting opposing current cases toward higher steepness values. Depth limited values for following waves and currents remained nearly unchanged between the two.

**Table 2.** Values of Breaking Parameters at Break Points

| Local Time | SWIFT | $\mathbf{u}\cdot\frac{\mathbf{k}}{k}$ (m/s) | $H_s$ (m) | $\bar{k}$ (rad/m) | d (m) | $\frac{\bar{k}H_s}{2}$ | $\frac{H_s\bar{k}}{\tanh(\bar{k}d)}$ | $\frac{H_s}{d}$ |
|---|---|---|---|---|---|---|---|---|
| 20 May 2012-12:37 | 04 | −0.71 | 0.66 | 0.45 | 3.5 | 0.15 | 0.32 | 0.19 |
| 20 May 2012-12:42 | 04 | −0.54 | 1.14 | 0.34 | 3.7 | 0.19 | 0.45 | 0.31 |
| 17 May 2012-11:07 | 06 | −0.74 | 0.48 | 0.62 | 3.0 | 0.15 | 0.31 | 0.16 |
| 17 May 2012-11:17 | 06 | −0.47 | 0.90 | 0.34 | 4.9 | 0.15 | 0.33 | 0.18 |
| 17 May 2012-12:02 | 06 | −0.36 | 0.96 | 0.34 | 2.9 | 0.16 | 0.44 | 0.34 |
| 18 May 2012-07:27 | 04 | 0.34 | 0.77 | 0.41 | 2.0 | 0.16 | 0.47 | 0.39 |
| 18 May 2012-07:47 | 04 | 0.40 | 0.94 | 0.38 | 1.8 | 0.18 | 0.60 | 0.52 |
| 18 May 2012-07:52 | 04 | 0.56 | 0.76 | 0.45 | 1.2 | 0.17 | 0.72 | 0.66 |
| 13 May 2012-12:57 | 04 | 0.51 | 0.74 | 0.42 | 2.1 | 0.15 | 0.44 | 0.35 |
| 13 May 2012-13:12 | 04 | 0.59 | 0.68 | 0.56 | 1.1 | 0.19 | 0.71 | 0.64 |
| 13 May 2012-13:17 | 04 | 0.59 | 0.56 | 0.68 | 0.7 | 0.19 | 0.83 | 0.77 |
| 13 May 2012-13:02 | 03 | 0.66 | 0.68 | 0.62 | 0.8 | 0.21 | 0.93 | 0.87 |
| 13 May 2012-13:07 | 03 | 0.85 | 0.64 | 0.57 | 1.0 | 0.18 | 0.73 | 0.67 |
| 12 May 2012-09:17 | 04 | −0.48 | 0.57 | 0.48 | 2.5 | 0.14 | 0.32 | 0.22 |

model, the parameters are expected to follow the relation $Q_b = \int W(H)\rho(H)\mathrm{d}H = (P/\gamma)^4/[(P/\gamma)^2+1]$, where $P$ is the steepness parameter. For the case of *Thornton and Guza* [1983], the steepness is expressed $P = H_{rms}/d$. Similarly, the *Chawla and Kirby* [2002] steepness is $P = H_{rms}\bar{k}/(\tanh(\bar{k}d))$. While this seems to be at odds with breaking at occurring at a constant steepness (i.e., equations (3) and (4)), it is the manifestation of a random wavefield with a distribution of broken waves. In this model, the exceedance of steepness, $P$, over the breaking constant, $\gamma$, directly predicts the fraction of breaking.

The correlations for the two breaking parameters are similar ($r^2 = 0.64$ and $r^2 = 0.62$, Figure 8). However, the sum of squared residuals on opposing currents is reduced by 36% when using the *Chawla and Kirby* [2002] steepness compared to the depth-only $H/d$, implying a more robust prediction of breaking on both depth limited and wave/current cases. The improvement in correlation is minimal because of large residuals associated with the minimally changed following wave and current cases. The increase in steepness can be seen in Table 2, which reports breaking parameter values at break points identified with large $Q_b$. The *Chawla and Kirby* [2002] steepness is increased on opposing waves and currents when compared to the depth limited steepness.

### 3.3. TKE Dissipation Rates

Average dimensional profiles of the turbulent dissipation rate are shown for breaking and nonbreaking points in Figure 9. Breaking cases show increased near surface turbulence, with qualitative similarities to the results of *Gemmrich* [2010], *Feddersen* [2012b], *Thomson* [2012], *Thomson et al*. [2013], and *Schwendeman et al*. [2014]. Averaging over all cases obscures the details specific to a given set of conditions, but it also shows the robustness of the breaking generated turbulence relative to the background levels (which are assumed to be advected from elsewhere in the inlet).

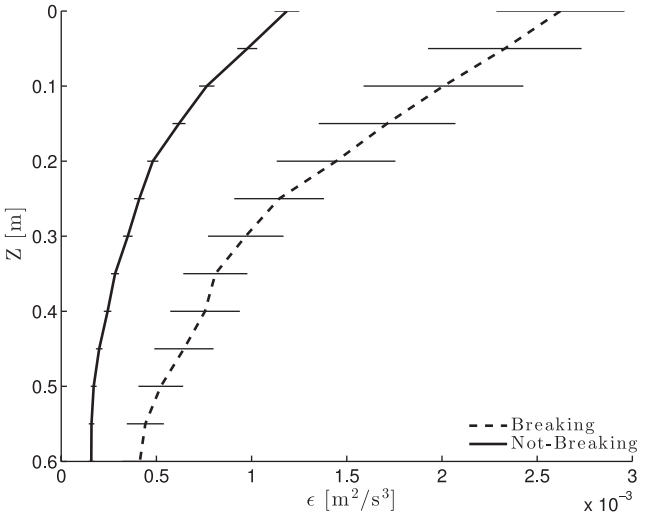


**Figure 9.** Mean breaking (dashed line) and nonbreaking (solid line) turbulent dissipation rates. Breaking cases are identified as two or more video identified breakers per 5 min burst, roughly corresponding to $Q_b > 0.02$. Horizontal lines show the standard error. Breaking cases show enhanced near surface turbulent dissipation when compared to background levels.

Nondimensional profiles of the turbulent dissipation rate are shown for individual break point observations in Figure 10. Figure 10a is the exponential surf zone scaling derived by *Feddersen* [2012b]. Figure 10b is the power law scaling introduced by *Terray et al*. [1996]

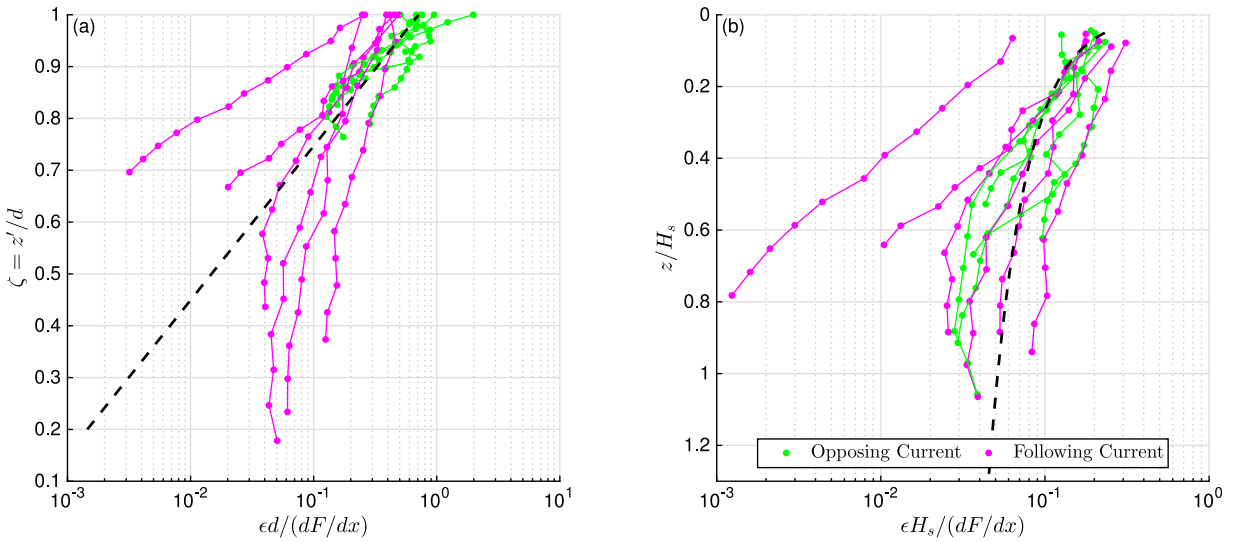


**Figure 10.** Turbulent dissipation rate scalings from (a) the exponential *Feddersen* [2012b] scaling, and (b) the modified *Terray et al*. [1996] power law scaling. Points where currents oppose waves are shown in green. Following waves and currents are shown in magenta. Of the 14 profiles for which two or more breakers were identified per 5 min burst, 11 had a forward differenced flux gradients d$F/$d$x$ that passed quality control. Each distinct profile has 13 dissipation estimates for a total $N = 143$. Because the *Terray et al*. [1996] scaling is undefined at $z'=0$, surface dissipation measurements are not used in the fit ($N = 132$). The exponential scaling has a greater correlation, with $r^2=0.54$ for the *Feddersen* [2012b] scaling compared to the $r^2=0.48$ for the *Terray et al*. [1996] scaling. Nonlinear fits are found using MATLAB's *fitnlm* function.

and adapted to the surf zone by *Feddersen* [2012b]. For each, the gradient of wave energy flux, $dF/dx$, is used to normalize the profiles. Of the 14 bursts with two or more breaking waves per 5 min burst ($n \geq 2$), 11 passed quality control ($dF/dx < 0$). Surface dissipation rates ($z = 0$) were excluded from the *Terray et al*. [1996] estimates, because the scaling asymptotes at the surface. Best fit curves were found using MATLAB's *fitnlm* function. By fitting each burst individually, errors in wave energy flux gradients are absorbed into the fitting parameters $A_F$, and $A_T$ (Table 3). However, because each profile has a small number of points ($n = 13$), the best fit parameters to all 11 bursts are also reported in Table 3, and plotted in Figure 10.

The exponential scaling by depth had improved skill over the power law scaling by wave height ($r^2=0.54$ compared to $r^2=0.48$). The exponential scaling was especially skillful for the individual following wave-current cases ($r^2 \geq 0.95$) when compared to the opposing cases ($r^2 \geq 0.87$). The best fit exponent for the power law scaling was $\lambda=-0.50$, which does not agree with the literature, where typically $\lambda=-2$ is found. By contrast, the two parameters in the *Feddersen* [2012b] scaling, $\alpha$ and $A_F$, were similar to the reported values in *Feddersen* [2012b]. Using the best fit for all data, $\alpha=7.7$ gives a theoretical $\tilde{A}_F=0.0035$. The implied percent of wave dissipation to TKE dissipation is then $A_F/\tilde{A}_F=0.089$, or 8.9%, similar to the 15% found in *Feddersen* [2012b].

While individual profile fits for the exponential scaling are more skillful with following currents, there is less variation between profiles with opposing currents such that correlations with all the opposing current points are larger than all the follow current points ($r^2=0.59$ to $r^2=0.52$). The decay scale for the best fit of the opposing current cases is more than twice that of the following current cases: $\alpha=9.4$, compared to $\alpha=4.4$. However, the implied wave dissipation to TKE dissipation ratio is similar between opposing and following cases (9.9% and 8.0%, respectively).

## 4. Discussion

The relation of currents to the modified steepness parameter of *Chawla and Kirby* [2002] is more clearly seen by using the linear phase speed $C=(g/\omega)\tanh(kd)$ and wave orbital velocity magnitude $|u_{orb}|=Hg/2C$:

$$\gamma=\frac{Hk}{\tanh(kd)}=\frac{Hg}{C^2}=\frac{2|u_{orb}|}{C}. \tag{22}$$

Using the *Mei* [1989] blocking limit of $-u=C/2$, the limiting steepness at the blocking point can be described as the ratio of wave orbital velocity to the mean current $\gamma=-4|u_{orb}|/u$. It is important to note

**Table 3.** Fitted Turbulent Dissipation Rate Scaling Parameters[a]

| | | | Exponential | | | Power Law | | |
|---|---|---|---|---|---|---|---|---|
| Local Time | SWIFT | Current | $A_F$ | $\alpha$ | $r^2$ | $A_T$ | $\lambda$ | $r^2$ |
| 20 May 2012-12:37 | 04 | Opposing | $2.3\times10^{-9}$ | 20 | 0.96 | $3.6\times10^{-2}$ | −0.74 | 0.98 |
| 20 May 2012-12:42 | 04 | Opposing | $4.0\times10^{-5}$ | 9.8 | 0.94 | $4.9\times10^{-2}$ | −0.49 | 0.82 |
| 17 May 2012-11:17 | 06 | Opposing | $2.2\times10^{-3}$ | 6.0 | 0.52 | $8.5\times10^{-2}$ | −0.22 | 0.29 |
| 17 May 2012-12:02 | 06 | Opposing | $3.8\times10^{-2}$ | 2.8 | 0.59 | $1.2\times10^{-1}$ | −0.22 | 0.48 |
| 18 May 2012-07:27 | 04 | Following | $1.6\times10^{-7}$ | 14 | 0.99 | $5.7\times10^{-3}$ | −0.92 | 0.88 |
| 18 May 2012-07:47 | 0 | Following | $2.2\times10^{-4}$ | 7.7 | 0.98 | $3.0\times10^{-2}$ | −0.66 | 0.81 |
| 13 May 2012-13:12 | 04 | Following | $5.2\times10^{-4}$ | 6.8 | 0.98 | $2.6\times10^{-2}$ | −0.82 | 0.96 |
| 13 May 2012-13:17 | 04 | Following | $8.8\times10^{-3}$ | 3.8 | 0.98 | $3.9\times10^{-2}$ | −0.79 | 0.96 |
| 13 May 2012-13:02 | 03 | Following | $3.2\times10^{-2}$ | 2.0 | 0.98 | $6.1\times10^{-2}$ | −0.44 | 0.87 |
| 13 May 2012-13:07 | 03 | Following | $4.5\times10^{-2}$ | 2.3 | 0.95 | $9.5\times10^{-2}$ | −0.49 | 0.93 |
| 12 May 2012-09:17 | 04 | Opposing | $3.4\times10^{-6}$ | 13 | 0.96 | $3.1\times10^{-2}$ | −0.74 | 0.94 |
| All ebbs | | | $7.7\times10^{-5}$ | 9.4 | 0.59 | $6.1\times10^{-2}$ | −0.43 | 0.56 |
| All floods | | | $4.3\times10^{-3}$ | 4.4 | 0.52 | $4.4\times10^{-2}$ | −0.57 | 0.44 |
| All breaking locations | | | $3.1\times10^{-4}$ | 7.7 | 0.54 | $4.3\times10^{-3}$ | −0.50 | 0.48 |

[a]Each individual fitted profile uses 13 data points for the *Feddersen* [2012b] exponential scaling and 12 data points for the adjusted *Terray et al.* [1996] power law scaling.

that $C$ and $u_{orb}$ are intrinsic variables, and would have to be adjusted for currents in the absolute reference frame. The practical application for a new parameter in the presence of opposing currents would use:

$$\gamma_u = \frac{Hg}{(C_a - 2u)^2}, \tag{23}$$

which approaches infinity near the blocking point. As breaking typically occurs before the blocking condition is reached, increasing $\gamma_u$ values would indicate increased probability of breaking.

Other aspects of the nearshore environment affect wave breaking besides currents. For example, adjustments to the depth limited $\gamma$ by beach slope and wave number has been shown to be important on some beaches [*Raubenheimer et al.*, 1996]. However, these adjustments did not significantly change the breaking parameter $\gamma$ or the wave dissipation models in this study. The $\gamma$ correction term for beach slope *Raubenheimer et al.* [1996] was small everywhere. Typical $\beta/(\bar{k}d)$ values at New River Inlet were 0.01, compared to a range of 0.1–1 in *Raubenheimer et al.* [1996]. Beach slope $\beta$ at New River Inlet, calculated as the gradient of the bathymetry provided by the Army Corps. of Engineers, was less than 0.1, and typically close to 0.02. The relatively small size of the gamma correction term when compared with *Raubenheimer et al.* [1996] is also due to higher centroid wave numbers. *Raubenheimer et al.* [1996] shows $1/(\bar{k}d)$ to range between 1 and 12, while $1/(\bar{k}d)$ values at identified break points at New River ranged from 0.2 to 1.2.

Although bottom slope effects are found to be small, several other factors might degrade the model-data comparison herein. The *Thornton and Guza* [1983] based wave dissipation models performance is possibly hindered by assuming a Rayleigh distribution. The CK2 model improves the original by including a current adjusted steepness parameter, and a length scale valid in intermediate depths, however still assumes a distribution that does not account for the increased kurtosis expected in focal zones [*Janssen and Herbers*, 2009]. The observations of wave transformation alongtrack are sensitive to variations with the 5 min ensembles and to errors in assuming that tracks are raypaths. Thus, the estimates of wave energy gradients, $dF/dx$, are noisy and may contaminate both the comparison to wave dissipation models and the evaluation of turbulence scaling.

Turbulence profiles in Figure 10a qualitatively follow the exponential scaling closely in the top 40% of the water column ($0.6 < \zeta \leq 1$), however scaled values in the lower water column deviate from the expected scaling. It is possible that the exponential scaling, which assumes a constant turbulent length scale, breaks down near the bottom boundary layer where turbulent length scales are typically assumed to increase linearly from the bed. *Feddersen* [2012b] found good agreement with the exponential scaling near the bed, but used observations with mean velocities to $U < 0.3$ m/s, where here surface velocities are $U \geq 0.6$ m/s. Breaking on opposing wave and currents was measured in deeper water, and therefore this effect is only seen for following wave and current cases. *Jones and Monismith* [2008] found the wave affected surface layer

transitioned directly into the bottom boundary layer in an estuarine embayment, with the transition typically in the bottom 10% of the water column. The much higher transition depth suggested by Figure 10a could be due to larger currents, however an estimate of bottom shear cannot be made from SWIFT observations, and therefore the expected transition depth proposed in *Jones and Monismith* [2008] is not quantified in this study.

## 5. Conclusions

Wave breaking is modulated by tidal currents at New River Inlet, such that waves break onshore in shallow water during flooding (following) currents and farther offshore in deeper water during ebbing (opposing) currents. Example SWIFT drifter data show images of breaking waves that correspond with decreases in wave energy flux and increased turbulent dissipation rates. Existing wave dissipation models adjusted for currents show improved correlations with measured energy flux gradients. Turbulent dissipation rate profiles are elevated in breaking regions and follow a proposed exponential scaling.

**Acknowledgments**

SWIFT data can be found at http://www.apl.washington.edu/swift. Funding for this project was provided by the Office of Naval Research. Thanks to the field engineers J. Talbert and A. de Klerk for their help developing the SWIFT drifters and collecting the field data. Thanks to C. Bassett, R. Carini, J. P. Rinehimer, and M. Schwendeman for helpful conversations. Thanks to B. Raubenheimer and S. Elgar for sharing data and providing feedback on the manuscript. Thanks to F. Feddersen and two anonymous reviewers for substantial efforts to improve this paper.

## References

Banner, M. L., A. V. Babanin, and I. Young (2000), Breaking probability for dominant waves on the sea surface, *J. Phys. Oceanogr.*, *30*, 3145–3160.

Battjes, J. A., and J. P. F. M. Janssen (1978), Energy loss and set-up due to breaking of random waves, Proceedings of 16th International Conference on Coastal Engineering, 569–587, Am. Soc. of Civ. Eng., N. Y.

Bowen, A. J., D. L. Inman, and V. P. Simmons (1968), Wave 'set-down' and set-up, *J. Geophys. Res.*, *73*(8), 2569–2577.

Chawla, A., and J. T. Kirby (2002), Monochromatic and random wave breaking at blocking points, *J. Geophys. Res.*, *107*(C7), doi:10.1029/2001JC001042.

Elgar, S., T. H. C. Herbers, V. Chandran, and R. T. Guza (1995), Higher-order spectral analysis of nonlinear ocean surface gravity waves, *J. Geophys. Res.*, *100*(C3), 4977–4983.

Feddersen, F. (2012a), Observations of the surf-zone turbulent dissipation rate, *J. Phys. Oceanogr.*, *42*, 386–399, doi:10.1175/JPO-D-11-082.1.

Feddersen, F. (2012b), Scaling surf zone turbulence, *Geophys. Res. Lett.*, *39*, L18613, doi:10.1029/2012GL052970.

Gallagher, E. L., S. Elgar, and R. T. Guza (1998), Observations of sand bar evolution on a natural beach, *J. Geophys. Res.*, *103*(C2), 3203–3215.

Gemmrich, J. (2010), Strong turbulence in the wave crest region, *J. Phys. Oceanogr.*, *40*, 583–595, doi:10.1175/2009JPO4179.1.

Herbers, T. H. C., N. R. Russnogle, and S. Elgar (2000), Spectral energy balance of breaking waves within the surf zone, *J. Phys. Oceanogr.*, *30*, 2723–2737.

Herbers, T. H. C., P. F. Jessen, T. T. Janssen, D. B. Colbert, and J. H. MacMahan (2012), Observing ocean surface waves with gps-tracked buoys, *J. Atmos. Oceanic Technol.*, *29*, 944–959.

Iverson, H. W. (1952), *Laboratory Study of Breakers, Gravity Waves, Circ. 52*, U.S. Bur. of Stand., Washington, D. C.

Janssen, T. T., and J. Battjes (2007), A note on wave energy dissipation over steep beaches, *Coastal Eng.*, *54*(9), 711–716, doi:10.1016/j.coastaleng.2007.05.006.

Janssen, T. T., and T. H. C. Herbers (2009), Nonlinear wave statistics in a focal zone, *J. Phys. Oceanogr.*, *39*(8), 1948–1964, doi:10.1175/2009JPO4124.1.

Jones, N. L., and S. G. Monismith (2008), The influence of whitecapping waves on the vertical structure of turbulence in a shallow estuarine embayment, *J. Phys. Oceanogr.*, *38*, 1563–1580, doi:10.1175/2007JPO3766.1.

Kirby, J. T. (1984), A note on linear surface wave-current interaction over slowly varying topography, *J. Geophys. Res.*, *89*(C1), 745–747.

Kolmogorov, A. N. (1941), Dissipation of energy in the locally isotropic turbulence, *Dokl. Akad. Nauk SSSR*, *30*, 301–305.

Lamarre, E., and W. K. Melville (1991), Air entrainment and dissipation in breaking waves, *Lett. Nat.*, *351*, 469–472.

Lippmann, T. C., and R. A. Holman (1990), The spatial and temporal variability of sand bar morphology, *J. Geophys. Res.*, *95*(C7), 11,575–11,590.

Longuet-Higgins, M. S. (1970), Longshore currents generated by obliquely incident sea waves: 1, *J. Geophys. Res.*, *75*(33), 6778–6789.

Méhauté, B. L., D. Divoky, and A. Lin (1968), Shallow water waves: A comparison of theories and experiments, Proceedings in *11th International Conference on Coastal Engineering*, vol. 1, pp. 86–107, Am. Soc. of Civ. Eng., London, U. K.

Mei, C. (1989), *The Applied Dynamics of Ocean Surface Waves*, World Sci., Teaneck, N. J.

Miche, A. (1944), Mouvements ondulatoires de la mer en profondeur croissante ou décroissante. forme limite de la houle lors de son déferlement. application aux digues maritimes. Troisième partie. Forme et propri es des houles limites lors du déferlement. Croissance des vitesses vers la rive. Ann. Ponts Chaussées, 114, pp. 369–406.

Olabarietta, M., J. C. Warner, and N. Kumar (2011), Wave-current interaction in Willapa Bay, *J. Geophys. Res.*, *116*, C12014, doi:10.1029/2011JC007387.

Orescanin, M., B. Raubenheimer, and S. Elgar (2014), Observations of wave effects on inlet circulation, *Cont. Shelf Res.*, *82*, 37–42, doi:10.1016/j.csr.2014.04.010.

Raubenheimer, B., R. T. Guza, and S. Elgar (1996), Wave transformation across the inner surf zone, *J. Geophys. Res.*, *101*(C10), 25,589–25,597.

Schwendeman, M., J. Thomson, and J. Gemmrich (2014), Wave breaking dissipation in a fetch-limited sea, *J. Phys. Oceanogr.*, *44*(1), 104–127.

Sénéchal, N. (2003), Etude de la propagation des vagues au-dessus d'une bathymétrie complexe en zone de surf, diss, Atelier national de reproduction des thèses.

Stokes, G. G. (1880), Considerations relative to the greatest height of oscillatory irrational waves which can be propagated without change of form, *Math. Phys. Pap.*, *1*, 225–228.

Terray, E., M. Donelan, Y. Agrawal, W. Drennan, K. Kahma, A. Williams, P. Hwang, and S. Kitaigorodskii (1996), Estimates of kinetic energy dissipation under breaking waves, *J. Phys. Oceanogr.*, *26*, 792–807.

Thomson, J. (2012), Wave breaking dissipation observed with SWIFT drifters, *J. Atmos. Oceanic Technol.*, *29*(12), 1866–1882, doi:10.1175/JTECH-D-12-00018.1.

Thomson, J., E. A. D'Asaro, M. Cronin, E. Rogers, R. Harcourt, and A. Schcerbina (2013), Waves and the equilibrium range at Ocean Weather Station P, *J. Geophys. Res. Oceans*, *118*, 5951–5962, doi:10.1002/2013JC008837.

Thornton, E. B., and R. T. Guza (1982), Energy saturation and phase speeds measured on a natural beach, *J. Geophys. Res.*, *87*(C12), 9499–9508.

Thornton, E. B., and R. T. Guza (1983), Transformation of wave height distribution, *J. Geophys. Res.*, *88*(C10), 5925–5938.

Wargula, A., B. Raubenheimer, and S. Elgar (2014), Wave-driven along-channel subtidal flows in a well-mixed ocean inlet, *J. Geophys. Res. Oceans*, *119*, 2987–3001, doi:10.1002/2014JC009839.

Wiles, P., T. P. Rippeth, J. Simpson, and P. Hendricks (2006), A novel technique for measuring the rate of turbulent dissipation in the marine environment, *Geophys. Res. Lett.*, *33*, L21608, doi:10.1029/2006GL027050.

Wright, L. D., and A. D. Short (1984), Morphodynamic variability of surf zones and beaches: A synthesis, *Mar. Geol.*, *56*, 93–118.